Effect of Part Thickness and Build Angle on the Microstructure, Surface Roughness, and Mechanical Properties of Additively Manufactured IN-939

A. FARDAN ⓘ, U. KLEMENT, H. BRODIN, and E. HRYHA

Powder bed fusion-laser beam of metals (PBF-LB/M) has attracted significant interest due to the possibility of producing dedicated design features like thin-walled structures, even though their mechanical response and microstructure are not well understood. Hence, thin-walled IN-939 structures of different thicknesses (0.5, 1 and 2 mm) were manufactured at two build angles (90 and 45 deg) by PBF-LB/M. A preferred $\langle 100 \rangle$ crystallographic orientation was found along the build direction in all cases. The crystallographic texture intensity and surface roughness increased as the part thickness decreased for 90 deg and increased for 45 deg build angle. Reduction in wall thickness resulted in a decrease in the tensile properties, *e.g.*, YS decreases by up to 33 pct and UTS decreases by up to 30 pct in comparison with the bulk specimen which had YS of 1051 ± 11 MPa and UTS of 1482 ± 9 MPa. Obtained results indicate that the apparent difference in tensile properties is primarily due to the overestimation of the load-bearing area. Two methods to estimate the accurate tensile properties based on roughness compensation are presented, using of which the corrected tensile performance of the thin-walled specimens was comparable with a standard tensile specimen.

I. INTRODUCTION

ADDITIVE Manufacturing (AM) is an emerging technology where the component is manufactured by an AM machine layer-by-layer from a 3D computer-aided design (CAD) file.[1] AM has enabled the fabrication of complex structures with intricate features which was not possible with traditional manufacturing techniques (such as casting, forging, or machining). This is enabled by the layer-by-layer manufacturing in AM where the material is only used where it is required leading to reduced material waste and shortened product development cycle.[2]

Powder bed fusion-laser beam of metals (PBF-LB/M)[3] is one of the most developed AM technologies. In PBF-LB/M, a layer of powder with a pre-defined layer thickness is deposited with the help of a re-coater. A laser beam is then used to selectively melt the region of interest. The melting can be done with different strategies of which stripe scan strategy is a common strategy. Stripe scan strategy divides the cross-sectional area to several stripes. Then the infill parameters are used to consolidate each stripe one-by-one. Once all the stripes are scanned, a contour scanning is implemented to reduce the surface roughness.[4] The process is then repeated over several layers until the required part is obtained. PBF-LB/M offers a high design freedom and has enabled lightweight products with novel lattice structures and organic designs.[5,6]

One alloy group which has been heavily researched in the last decade is Ni-base superalloy. These alloys are high-temperature and high-performance alloys used primarily in the aerospace and gas turbine industry.[7] PBF-LB/M creates value by having complex geometries with additional functionalities like increased heat transfer in turbine components enabled by cooling channels or wavy microchannels.[5,7] Inconel 939 (IN-939) is a γ'-strengthened Ni-base superalloy and one of the earliest Ni-base superalloys adopted for PBF-LB/M.[8] This alloy offers corrosion and oxidation resistance and retains mechanical properties owing to the precipitation strengthening by γ'. It was initially developed as casting

A. FARDAN, U. KLEMENT, and E. HRYHA are with the Department of Industrial and Materials Science, Chalmers University of Technology, 412 96 Göteborg, Sweden. Contact e-mail: fardan@chalmers.se H. BRODIN is with the Department of Industrial and Materials Science, Chalmers University of Technology and also with the Siemens Energy AB, 612 83 Finspång, Sweden.

for applications in blades and vanes of gas turbines for temperatures up to 850 °C.[9]

Ni-base superalloys are cast with a minimum wall thickness of ~ 1.5 to 2.5 mm in aerospace applications.[10,11] While in PBF-LB/M, it is possible to manufacture components with a minimum wall thickness of ~ 0.3 to 0.4 mm.[12] This has made PBF-LB/M components attractive for aerospace industry; however, mechanical behavior of components with such thin walls is unknown, leading to high safety factors in design. Additionally, surface roughness of as-built thin walls adds to the complexity.

Previously, studies have been dedicated to studying the thin-wall effect in FCC (face-centered cubic) materials like stainless steel 316L (SS316L)[4,13–15] and Hastelloy X (HX).[16–18] Leicht et al.[4] studied the microstructure and crystallographic texture of SS316L in as-built condition with the part thickness varying from 0.2 to 3.0 mm as well as with build angles of 30 (with supports) and 45 deg (without supports). Large elongated grains with preferential ⟨110⟩ orientation were found which was attributed to the thermal gradient along the build direction. Also, small grains with random orientations were found closer to the surface. A follow-up study was done by Leicht et al.[13] to study the effect of part thickness on tensile properties for SS316L. The microstructure between the 1 and 3 mm thick samples was not different; however, the tensile properties of the 1 mm sample were inferior to the 3 mm sample. The tensile properties of the 3 mm sample were comparable to that of the standard specimen with 5.72 mm thickness. Furthermore, the thickness of the cross-sectional area was measured from light optical microscope images with only considering bulk thickness and excluding the surface roughness. Wang et al.[14] studied the microstructure–property relation of SS316L for strut diameter ranging from 0.25 to 5 mm. The superior tensile performance of thicker struts was attributed to the strong ⟨110⟩ texture that promoted the twinning-induced plasticity (TWIP). This led to a better combination of strength and ductility compared to that of thinner strut with strong ⟨100⟩ texture or weak ⟨110⟩ texture. A detailed study was done by Wang et al.[15] on SS316L thin strut (0.25 mm) with single crystalline-like microstructure with ⟨110⟩ texture parallel to the build direction. The same effect was observed here, i.e., twinning-induced plasticity (TWIP) which led to a good combination of strength and ductility.

Sanchez-Mata et al.[16] studied microstructure–property relations of HX with strut diameters ranging from 0.25 to 2 mm. Unlike SS316L, the crystallographic texture was primarily ⟨110⟩ except for transition from fiber texture to single crystal when strut diameter is reduced from 2 to 0.25 mm. The tensile behavior was similar where the thick strut diameter had better combination of strength and ductility than thin struts.

Yu et al.[17] studied microstructure–property relations of HX with thickness ranging from 1 to 4 mm. The dominant texture was ⟨110⟩ along the build direction, which was consistent with the texture analysis by Sanchez-Mata et al.[16] Yu et al.[17] presented tensile performance before and after roughness calibration. The yield and tensile strength after applying the calibration were similar for samples of varying thickness. The texture measurement performed by Yu et al.[18] using neutron diffraction showed a different texture behavior to previous works[16,17] as the part thickness is reduced. The texture changed from ⟨110⟩ to ⟨100⟩ when the part becomes thinner which again was attributed to the thermal gradient caused by the differences in the geometry.

The present study aims to explore the role of part thickness and build angle on microstructure and tensile properties to develop design guidelines for PBF-LB/M of IN-939. This is done by studying the microstructure of PBF-LB/M processed IN-939 walls of different thicknesses (0.5 to 2 mm) in the as-built and heat-treated state. The focus was on the microstructure study consisting of evaluation of crystallographic texture and grain characteristics using electron back scatter diffraction (EBSD). This was followed by tensile testing and surface roughness analysis of heat-treated parts. Furthermore, a comparison was made between thin-wall components and a standard bulk specimen. The study is believed to be beneficial for designers of PBF-LB/M as it will aid in understanding the relation of part thickness and build angle to tensile response and prevent in overdesign of thin-walled components.

II. MATERIAL AND METHODS

A. Material

Gas-atomized IN-939 with a particle size range of 15 to 45 μm was provided by Höganäs AB (Höganäs, Sweden) as feedstock material. The nominal chemical composition of IN-939 powder is provided in Table I. An EOS M290 (Electro Optical Systems GmbH, Krailling, Germany) Machine was used to produce the parts. This system has a Yb-fiber laser with a maximum power of 400 W and a focus diameter of 100 μm. The parts were produced with a layer thickness of 40 μm utilizing in-house developed process parameters with a striped strategy having a scan rotation of 67 deg at Siemens Energy AB (Finspång, Sweden). The parts of different thicknesses (0.5, 1, and 2 mm) and build angles (90 and 45 deg) were fabricated. The parts underwent hot isostatic pressing (HIP) at 103 MPa with Argon (Ar) atmosphere followed by vacuum heat treatment (HT). The HIP and HT conditions are provided in Table II. Additionally, a part with a diameter of 12 mm with a

Table I. Chemical Composition of IN-939 Powder Used in This Study

Cr	Co	C	W	Nb	Ta	Ti	Al	Zr	B	Ni
22.1	19.2	< 0.01	2.0	1.0	1.5	3.8	1.9	0.02	0.004	bal

Table II. HIP and HT Conditions for IN-939

Step	Temperature (°C)	Time (Hours)	Heating Rate (°C/h)	Cooling Rate (°C/h)
HIP	1190	4	< 10	< 10
Solution Treatment	1160	4	< 25	20 to 40
1st Aging	1000	6	< 25	20 to 40
2nd Aging	900	24	< 25	20 to 40
3rd Aging	700	16	< 25	rapid cool with Ar

length of 120 mm (hereafter referred as 'Standard') with 90 deg build angle was built for comparison.

B. Microstructural Characterization

The cross-section along the build direction (BD) was used for metallographic investigation. The cross-section for investigation was obtained from the bottom of the component shown in Figure 1. The samples were mounted in conductive bakelite resin and ground using SiC papers (#120, #220, #320, #500, #800, and #1200). This was followed by successive polishing using diamond suspension of 3, 1, and 0.25 μm. A final step of mechanical polishing using 0.05 μm colloidal silica was carried out. The force applied and the duration of grinding/polishing steps are similar to the recommended values by Struers (Roper Technologies, Copenhagen, Denmark).

Electrochemical etching in 10 wt pct oxalic acid at 3 V for 3 seconds was carried out to reveal the solidification structure. Electrolytic etching using 10 pct phosphoric acid at 10 V for 5 seconds was used to etch the γ matrix and reveal the γ' and carbide/boride particles. Light optical microscopy (LOM) was performed for low-resolution analysis. Scanning electron microscopy was performed in a Leo Gemini 1550 SEM for high-resolution analysis. Texture and grain size analyses were performed by using electron backscatter diffraction (EBSD) technique using a Nordlys II detector (Oxford Instruments, Abingdon, Oxfordshire, England). The measurements were performed at an accelerating voltage of 20 kV using 60 μm aperture with a step size of 2.5 μm. The length of the analyzed area was constant with a height of 1500 μm and the width changed based on the thickness of the sample. A data clean-up was carried out in Aztec Crystal software, consisting of removing wild spikes and performing noise reduction (7 nearest neighbors required). EBSD data analysis was performed using an open-source MATLAB toolbox MTEX (version 5.8.0).[19] The pole figures are plotted using equal area projection, contoured with a half-width of 10 deg, and scaled in multiples of random density (MRD). The inverse pole figure maps (IPF) are plotted with respect to the build direction (BD).

C. Tensile Testing

The tensile testing was performed only on specimens extracted from heat-treated parts at room temperature. The dimensions of the tensile test specimens were a modified version as described in details elsewhere.[18] The dimensions of the specimen and the extraction locations using electrical discharge machining (EDM)
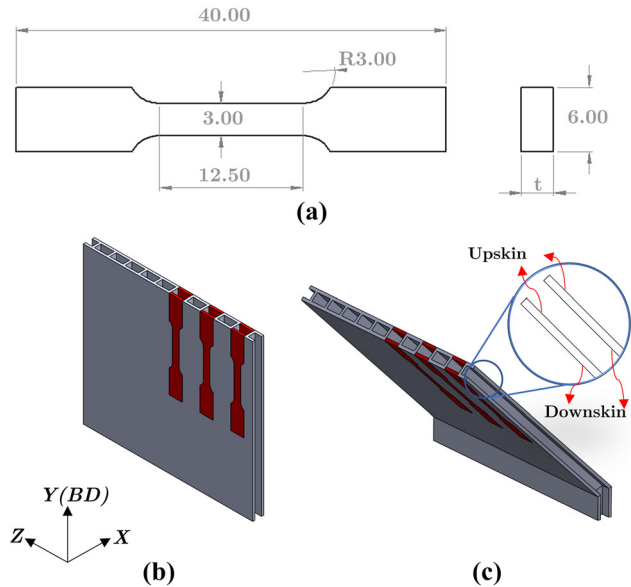

Fig. 1—(a) Dimensions of miniature tensile specimens. All dimensions are in mm, (b) Extraction of tensile specimens from the part fabricated with 90 deg build angle, (c) Extraction of tensile specimens from the part fabricated with 45 deg build angle. BD is build direction.

are shown in Figure 1. Upskin and downskin are two terminologies commonly used in powder bed fusion community. Upskin refers to the upward facing surface and downskin refers to the downward facing surface. Both upskin and downskin are labeled in Figure 1(c). Mechanical testing was performed using an Instron 5500R with extension control of 3.50×10^{-3} mm s^{-1} (which is equivalent to a strain rate of 2.8×10^{-4} s^{-1} for a gauge length of 12.5 mm). The strain was obtained by using an axial extensometer (Epsilon Technology Group, Jackson, WY, USA) with a maximum span of 10 mm. The extensometer was kept on the sample until fracture occurred. The specimens were gripped with serrated wedges with a pressure of 200 bar. Yield strength (YS) with 0.2 pct strain offset ultimate tensile strength (UTS) and elongation to fracture were reported for the specimens. The total elongation to fracture is the strain at fracture obtained from the extensometer. At least, three tensile tests were conducted for each configuration. The thickness of the bars was measured using three different methods. Method 1 consisted of measuring the thickness and width using a digital caliper, which is a standard method for tensile testing. Method 2 was to measure the thickness of the specimen cross-sections with LOM. The thickness only included the bulk by

excluding the surface roughness zone. This was done once for a certain thickness and build angle which led to 6 measurements. Method 3 consisted of obtaining the bulk thickness by performing surface roughness measurements. The surface roughness was measured on both the sides of the specimen and the sum of both was the "thickness of the roughness." The roughness was then subtracted from the caliper measurement from Method 1. The details of the surface roughness measurements can be found in Section II–D. Tensile test data of a 'Standard' specimen (Figure 2) which was tested under similar conditions at Siemens Energy AB (Finspång, Sweden) are used for comparison purposes. The 'Standard' specimen was machined, and it had a relatively smoother surface than the miniature specimens. Therefore, the thickness was measured only using the caliper (Method 1).

D. Surface Roughness

The surface roughness was measured using confocal microscopy with a Sensofar S Neox instrument equipped with an objective lens of Nikon – EPI 20X. The roughness measurement was performed over a 3×2.2 mm surface in the center of both the sides of miniature tensile specimens in the gauge section with a lateral resolution of $0.64\ \mu$m. The processing consisted of a form removal of 2nd-order polynomial and filtration using a 5×5 spatial median noise reduction. The non-measured points were filled in and the level was set to the least-square planes. In this study, the 3D topography of the surface, the arithmetical mean height (S_a) and the root mean square height (S_q), and the core height (S_k) will be presented for different conditions in accordance with ISO 25718-2 standard.[20]
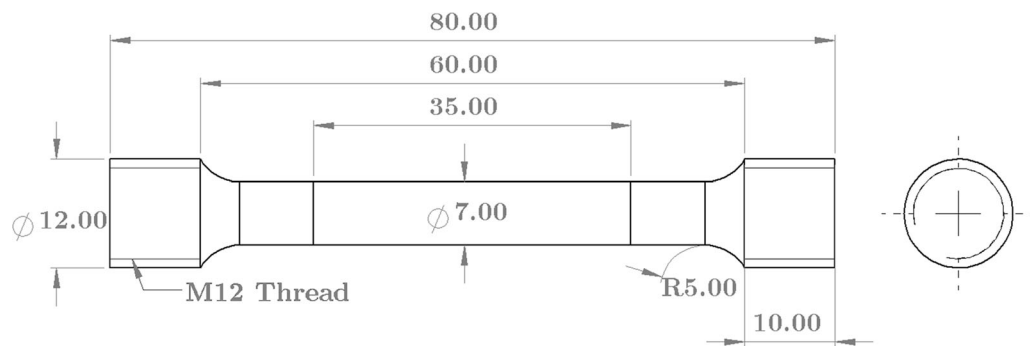

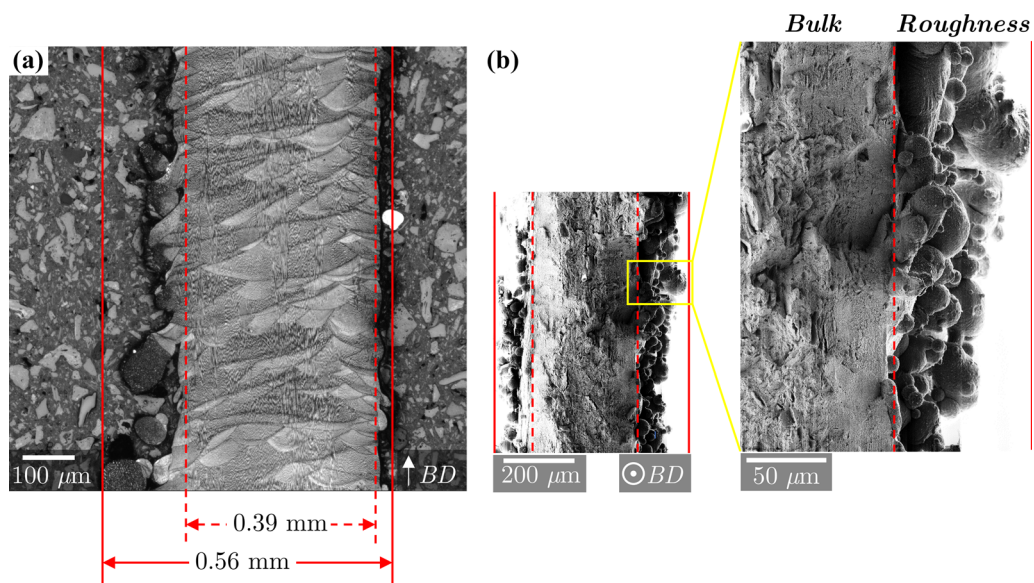Fig. 2—Dimensions of 'Standard' tensile specimens. All dimensions are in mm.

Fig. 3—(a) Light optical microscope (LOM) image of a part with 0.5 mm thickness. The solid line indicates the thickness including the roughness, while the dashed line indicates the bulk thickness, (b) Fracture surface of the tensile specimen showing the surface roughness and bulk regions. BD is build direction.
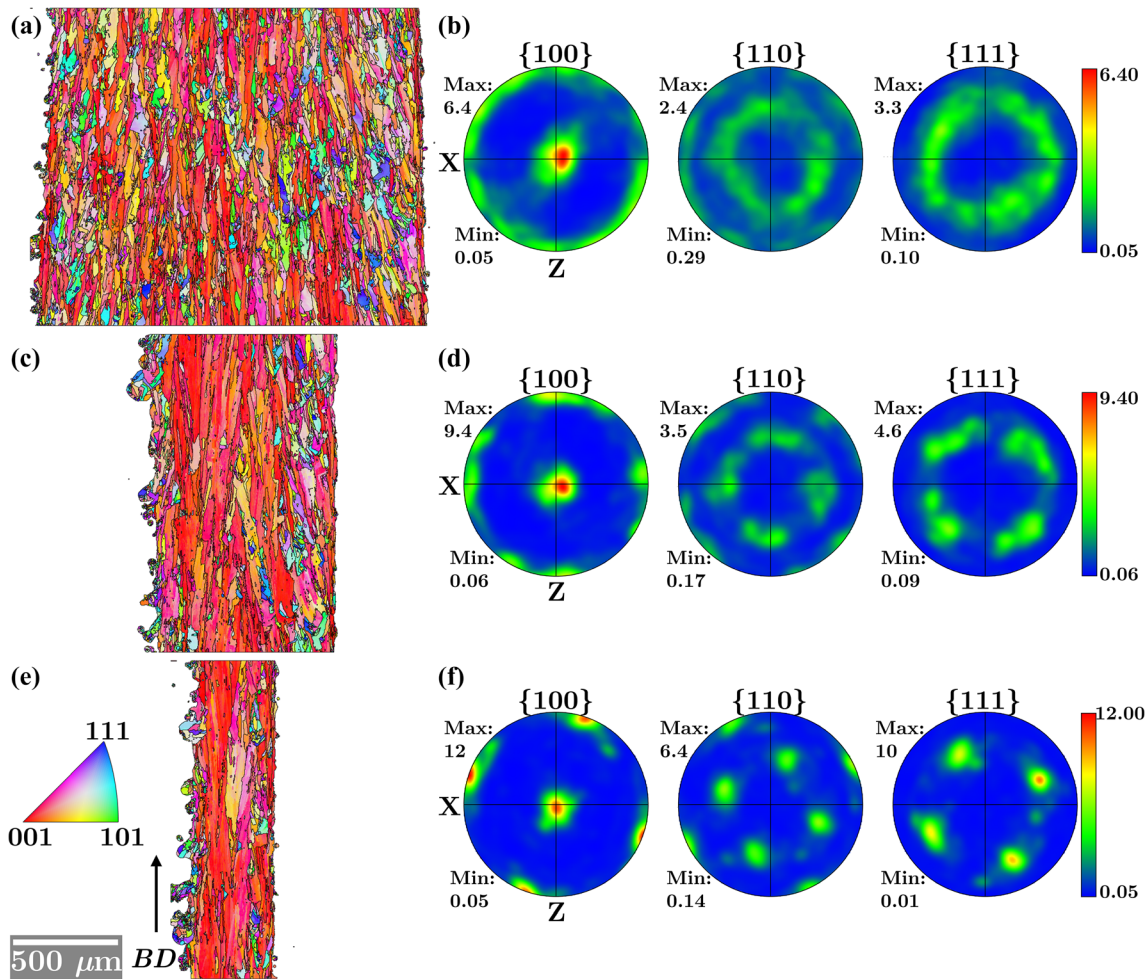
Fig. 4—EBSD orientation maps in inverse pole figure representation and the corresponding pole figures of IN-939 in as-built condition with 90 deg build angle of different thicknesses: (*a*, *b*) 2 mm thickness, (*c*, *d*) 1 mm thickness, and (*e*, *f*) 0.5 mm thickness. BD is build direction. BD is in the center for the pole figures. The orientation map is shown along BD and is given in IPF coloring. The color bar refers to the intensity of the pole figure (For interpretation of the references to color in this figure legend, the reader is referred to the web version of this article).

III. RESULTS AND DISCUSSION

A. *Microstructure and Texture in As-Built Condition*

The LOM image (Figure 3(a)) shows the microstructure of IN-939 in as-built condition. The microstructure consists of melt pool boundaries observed as half-circles, which is characteristic of PBF-LB/M process.[5] The non-uniform distribution of melt pool boundaries arises from the 67 deg scan rotation. The presence of semimelted and/or unmelted powder particles is observed closer to the surface which contributes to the surface roughness. As observed in LOM, the surface roughness is more pronounced on one side. This is caused by the different conditions faced by both the surfaces during part handling which will be discussed in detail later. The porosity in the as-built samples consisted of gas porosity and some occasional lack of fusion voids. The area fraction of porosity was about 0.1 pct.

The EBSD orientation maps in inverse pole figure representation of IN-939 with 90 deg build angle and the corresponding pole figures are shown in Figure 4. The black lines in the orientation maps indicate grain

boundaries with a misorientation greater than 10 deg and this is the same for all the EBSD orientation maps throughout this study. All the orientation maps are plotted along the BD (*Y*). The pole figures are plotted in the *XZ* projection plane, and the BD (*Y*) is in the center of the pole figure. The orientation maps show that columnar grains with several hundred microns in length are present in the microstructure. As seen from the inverse pole figure color coding and from the pole figures, they have a dominant orientation of ⟨100⟩ along the BD (*Y*). The intensity of ⟨100⟩ parallel to the BD increases as the thickness is reduced from 2 to 0.5 mm. This is, however, also related to the area analyzed. In the 0.5 mm sample, by far less grains are included in the analyzed area, which are then dominating the texture. The presence of ⟨100⟩ fiber texture is observed for thickness of 2 mm (Figure 4(b)). As the thickness decreases to 1 mm (Figure 4(d)), a ⟨100⟩ partial fiber texture is obtained. Finally, for the 0.5 mm thickness (Figure 4(f)), the partial fiber is replaced by a cube-like texture. The change from fiber to cube-like texture when thickness is reduced is probably due to the difference in

Table III. EBSD Grain Size Measurement of As-Built and Heat-Treated IN-939 with Different Thicknesses (0.5, 1, and 2 mm) and Build Angles (90 and 45 Deg)

Condition	Thickness (mm)	Build Angle (Deg)	No. of Grains (—)	Area-Weighted Mean (μm)	Min (μm)	Max (μm)
				Fitted Ellipse Major Length Axis		
As-Built	0.5	90	570	176.92	9.36	653.8
	1	90	1475	211.5	9.57	840.74
	2	90	3146	144.33	9.06	621.93
	0.5	45	1400	125.97	9.56	482.27
	1	45	2661	164.85	9.53	538.29
	2	45	3058	196.45	9.36	695.46
Heat-Treated	0.5	90	467	155.64	9.85	398.62
	1	90	1072	164.21	10.03	777.33
	2	90	2279	167.62	9.36	619.19
	0.5	45	1465	111.08	9.06	379.19
	1	45	2033	219.19	9.36	697.96
	2	45	3609	181.97	9.36	648.17
Standard Heat-Treated	12	90	3854	189.11	9.85	847.36

The measurement excluded the border grains*SD* standard deviation

heat accumulation. The heat accumulation is higher in the thin samples due to the cross-section of the area melted during the PBF-LB process. Again, when discussing the texture change, it is important to note the area analyzed and the number of grains, which decreases significantly from the 2 mm sample to the 0.5 mm sample (Table III), which also contributes to the sharper texture. The observed texture in IN-939 is different compared to that of other FCC materials in previous studies. For HX, the dominant grain orientation remained to be ⟨110⟩ parallel to BD for thickness ranging from 2 to 0.25 mm.[16] For SS316L, as the part thickness was reduced from 2 to 0.25 mm, the dominant grain orientation changed from ⟨110⟩ to ⟨100⟩ parallel to BD,[14] while studies by Leicht *et al*.[4,13] concluded that ⟨110⟩ is the dominant orientation for thicknesses from 0.2 to 3 mm. In a neutron diffraction study on HX, Yu *et al*.[18] reported the transition from ⟨110⟩ to ⟨100⟩ as the part thickness reduced from 4 to 1 mm. Studies which studied texture on bulk components for Ni-base superalloys such as IN-718[21,22] and IN-939[21,23] found 100⟩ along the BD to be the dominant orientation which is similar to this study. The difference in texture behavior could arise from the processing conditions (such as laser power, spot size, scan speed, hatch distance, and scan strategy) which could affect the volumetric energy density and thermal gradient during solidification which ultimately could have led to different grain growth directions. It could be stated that for IN-939 ⟨100⟩ was the energy favorable crystallographic direction caused by the thermal gradient along the build direction which led to the strong ⟨100⟩ texture.

The combined effect of different thicknesses at 45 deg build angle can be observed from the inverse pole figure orientation maps and pole figures in Figure 5. The 45 deg build angle was chosen for this investigation as it is the lowest angle possible to build without the need for support structures with necessary robustness and quality. From the initial observations, it is seen that the predominant grain orientation is ⟨100⟩ parallel to the

BD which is similar to the 90 deg specimens. However, the texture intensity is found to decrease as the thickness decreases as observed from the pole figures in Figure 5, which is in contrast to the behavior of the 90 deg specimens. This is partly related to the appearance of small grains at upskin and downskin that have orientations other than ⟨100⟩ . The influence of these grains on the overall texture becomes more pronounced the thinner the part thickness and the smaller the area analyzed (fewer elongated grains with ⟨100⟩ orientation in the center in the 0.5 mm sample which is also reflected in the slightly more random texture).

The reason for the apparent difference in texture mostly arises from the difference in thermal gradient and its direction during solidification process (heat dissipation) caused due to the change in thickness and build angle. The area of the EBSD analysis could also lead to the apparent difference in texture caused due to the number of grains analyzed. A schematic of the probable heat dissipation mechanisms for thin and thick walls with 90 and 45 deg build angles are shown in Figure 6. For thin walls with 90 deg build angle, the heat dissipation will be mostly conduction-based along the bulk material parallel to the but the BD (indicated by the straight arrows in Figure 6) while some minor dissipation to the surrounding powder could be possible (indicated by arrows which are straight and then bend toward the attached powder in Figure 6). This is due to the higher thermal conductivity of the bulk material than the powder. The powder bed is a good insulator which is caused by the limited contact between the powder particles and the insulating air gaps between the powder particles.[24–26] The thermal conductivity of HX in bulk and powder is used for discussion purposes due to the non-availability of thermal conductivity measurements for IN-939.[27] At room temperature, the thermal conductivity of bulk and powder is 10.39 W/m K and 0.02 W/m K, respectively. The thermal conductivity increases for the bulk to about 30 W/m K when the temperature is increased to 1227 °C while it
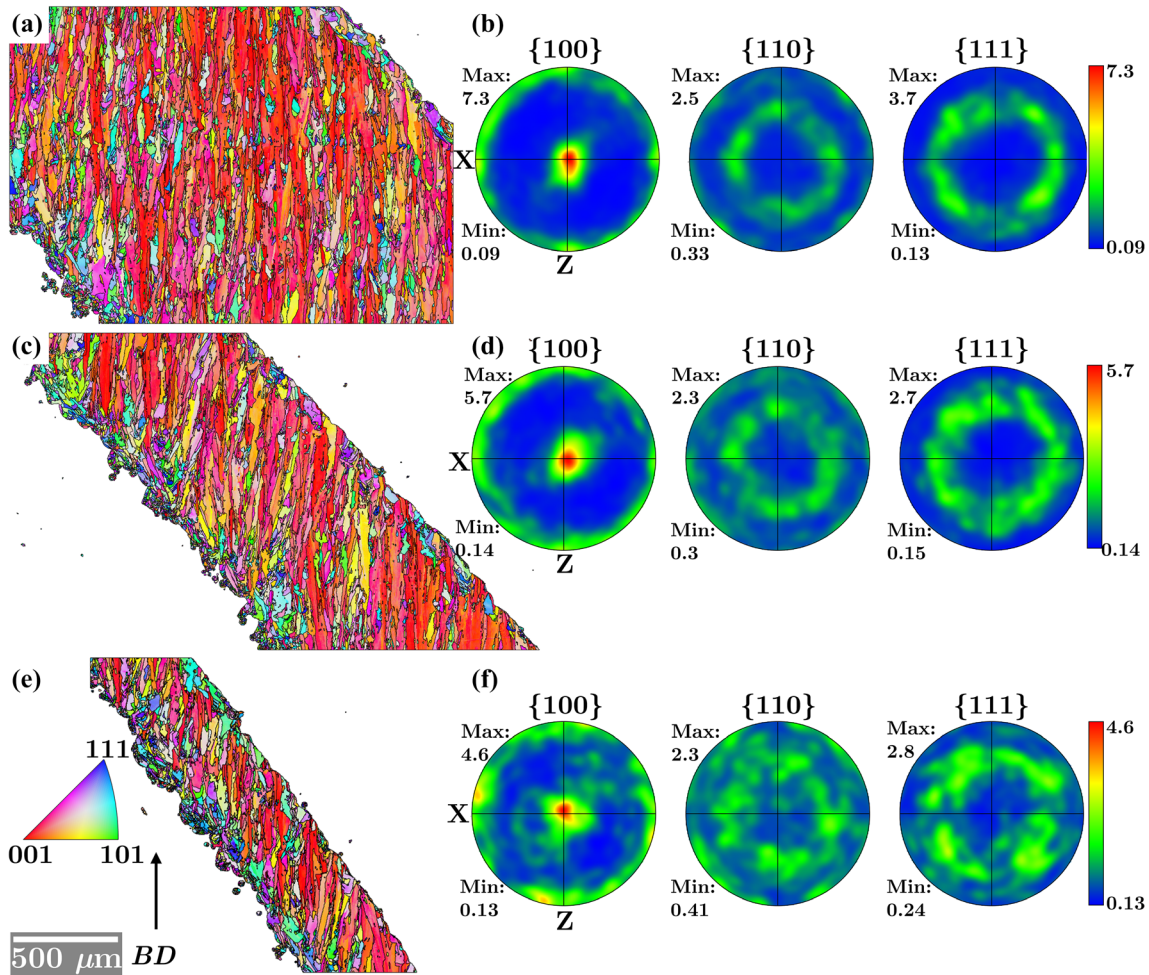
Fig. 5—EBSD orientation maps in inverse pole figure representation and the corresponding pole figure of IN-939 in as-built condition with 45 deg build angle of different thicknesses: (*a*, *b*) 2 mm thickness, (*c*, *d*) 1 mm thickness, and (*e*, *f*) 0.5 mm thickness. BD is build direction. BD is in the center for the pole figures. The orientation map is shown along BD and is given in IPF coloring. The color bar refers to the intensity of the pole figure (For interpretation of the references to color in this figure legend, the reader is referred to the web version of this article).
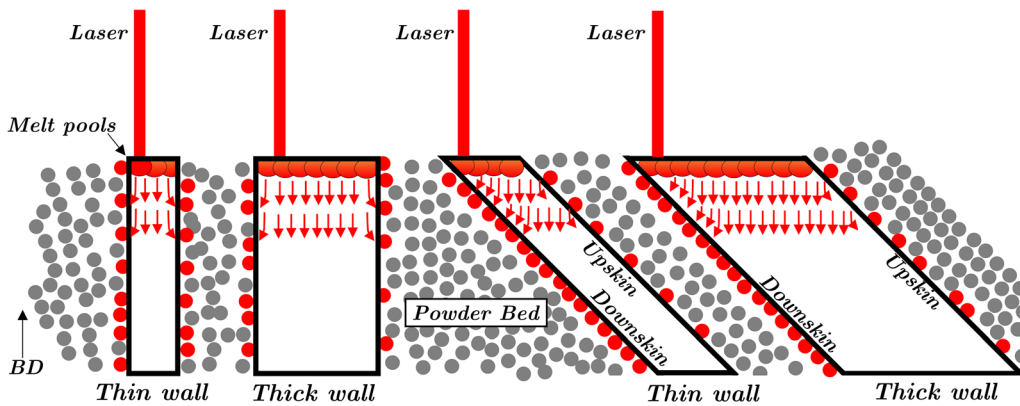

Fig. 6—Schematic explanation of the heat dissipation in thin and thick walls with 90 and 45 deg build angle. The red spheres represent the powder particles attached to the part. The red arrows indicate the direction of heat dissipation. BD is build direction (For interpretation of the references to color in this figure, the reader is referred to the web version of this article).

approximately remains the same for the powder at 0.02 W/m K. This strengthens the argument that the heat dissipation is mostly in conduction mode through the bulk into the build plate, hence the grain growth occurs along the BD, resulting in columnar grains with preferential orientation of ⟨100⟩. For thick walls with

90 deg build angle, heat dissipation is primarily through the bulk. But for thin wall with 45 deg build angle, there is still some restricted heat dissipation along the BD. The restriction arises from the 45 deg build angle and the heat dissipation condition is drastically different to that of 90 deg build angle. At 45 deg build angle, the heat dissipation is worse along the BD for the thin walls because of the powders below the downskin which has poor thermal conductivity. This leads to some small grains with random orientations to form in the downskin (Figure 5(e)). However, it is important to emphasize that some position of these fine grains is caused by partly melted/sintered particles to the downskin due to the higher heat accumulation, especially in case of thin-wall samples. But as the thickness increases for 45 deg build angle, the heat dissipation is improved and leads to the columnar growth of grains with a preferred orientation along the BD. The presence of small grains is also observed on the upskin for the 45 deg build angles. This could have possibly arisen from the effect of contour scan which occurs after the infill scan. During the PBF-LB/M process, the infill scan occurs first which melts and consolidates the entire cross-sectional area. This is followed by a contour scan where the perimeter is exposed with a thickness same as the melt pool to reduce surface roughness or reduce porosity. The width of these small grains is about the same size as the melt pool indicating that they could have formed due to the melting of fine-grained powder particles during the contour scan. Similar small grains near the surface were also reported in a study by Pant et al.[28] for IN-718 when contour scan was used.

B. Microstructure and Texture in Heat-Treated Condition

Analysis of the unetched microstructure after HIP + HT revealed that the porosity was approximately 0.01 pct. This shows that the HIP was effective in reducing the porosity. The etched microstructure of IN-939 in heat-treated condition is shown in Figure 7. To reveal the microstructure, samples were etched electrolytically with 10 pct phosphoric acid to remove the γ matrix. The microstructure consists of γ' precipitates and some grain boundary carbides. The presence of some intragranular carbides was also observed. The initial analysis showed that the microstructural features were similar irrespective of the thickness and build angle. The size of the γ' precipitates was 235.01 ± 37.52, 234.36 ± 26.18, and 241.59 ± 21.16 nm for specimens with thickness of 0.5, 1, and 2 mm, respectively. A study by Shaafi et al.[29] on PBF-LB/M IN-939 showed that the γ' precipitate can range from 100 to 200 nm based on SEM analysis. Another study by Banoth et al.[23] found the size of γ' precipitates to be ~ 40 to 50 nm when using TEM for both PBF-LB/M and cast IN-939 with similar heat treatment. The difference in γ' precipitate size arises due to the difference in heat treatment. The heat treatment in the study by Banoth et al.[23] consisted of a solution heat treatment followed by aging, while the study by Shaafi et al.[29] used a heat treatment which was the same as in this study. Therefore, it is seen that the γ' precipitate size
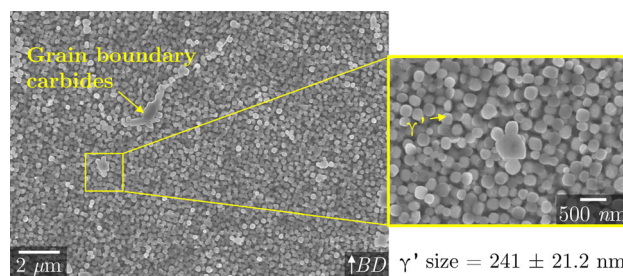

Fig. 7—SEM micrograph showing the microstructure of IN-939 in heat-treated condition (part thickness of 2 mm). BD is build direction.

can be affected by the type of heat treatment and in turn might affect the mechanical properties. However, for this study, it is seen that the size of γ' precipitate is similar and will not cause any differences in the tensile performance.

The EBSD orientation maps in inverse pole figure representation of heat-treated IN-939 with 90 deg build angle and the corresponding pole figures are shown in Figure 8. As can be seen, the strong $\langle 100 \rangle$ intensity parallel to the BD which was observed in the as-built condition (Figure 4) remains after heat treatment. Interestingly, the left-hand side of the samples shows a more random orientation appearance. This is most pronounced in the 2 mm sample, while less pronounced in the 0.5 mm sample. This random orientation arises from the grains which are in the vicinity of the edge which had less sintered/partially melted powder particles. This was also observed for the as-built samples (Figure 4). In the 0.5 mm sample, these powder particles have a larger influence due to their relatively larger fraction in relation to the sample cross-section while for the 2 mm sample, they do not have a significant influence which ultimately leads to a more random orientation. Similar to the as-built condition, the transition from fiber to partial fiber and finally cube-like components texture is observed when thickness is reduced from 2 to 0.5 mm which is similar to the as-built condition. The EBSD orientation maps (in inverse pole figure representation) of the heat-treated IN-939 with 45 deg build angle and the corresponding pole figures are shown in Figure 9. A strong $\langle 100 \rangle$ intensity parallel to the BD is observed for the specimens of all thicknesses studied. It is observed that the influence of heat treatment on texture is minimal for both 90 and 45 deg build angles. As in the as-built condition, small grains of random orientation can be seen at the upskin and downskin. After the heat treatment, these small grains are noticed to be slightly larger in size. In comparison, it is easier for the small grains than for the long columnar grains to recover, recrystallize, and undergo grain growth to reduce the internal stored energy. This is primarily the reason for these small grains in the 45 deg build angle sample to increase in size from ~ 35.25 to 88.47 μm after heat treatment.

The EBSD orientation maps (inverse pole figure representation) of the 'Standard' IN-939 bulk specimen in heat-treated condition with 90 deg build angle and the corresponding pole figures are shown in Figure 10. The presence of a $\langle 100 \rangle$ preferred orientation parallel to the BD is observed. It can be found that even after increase of
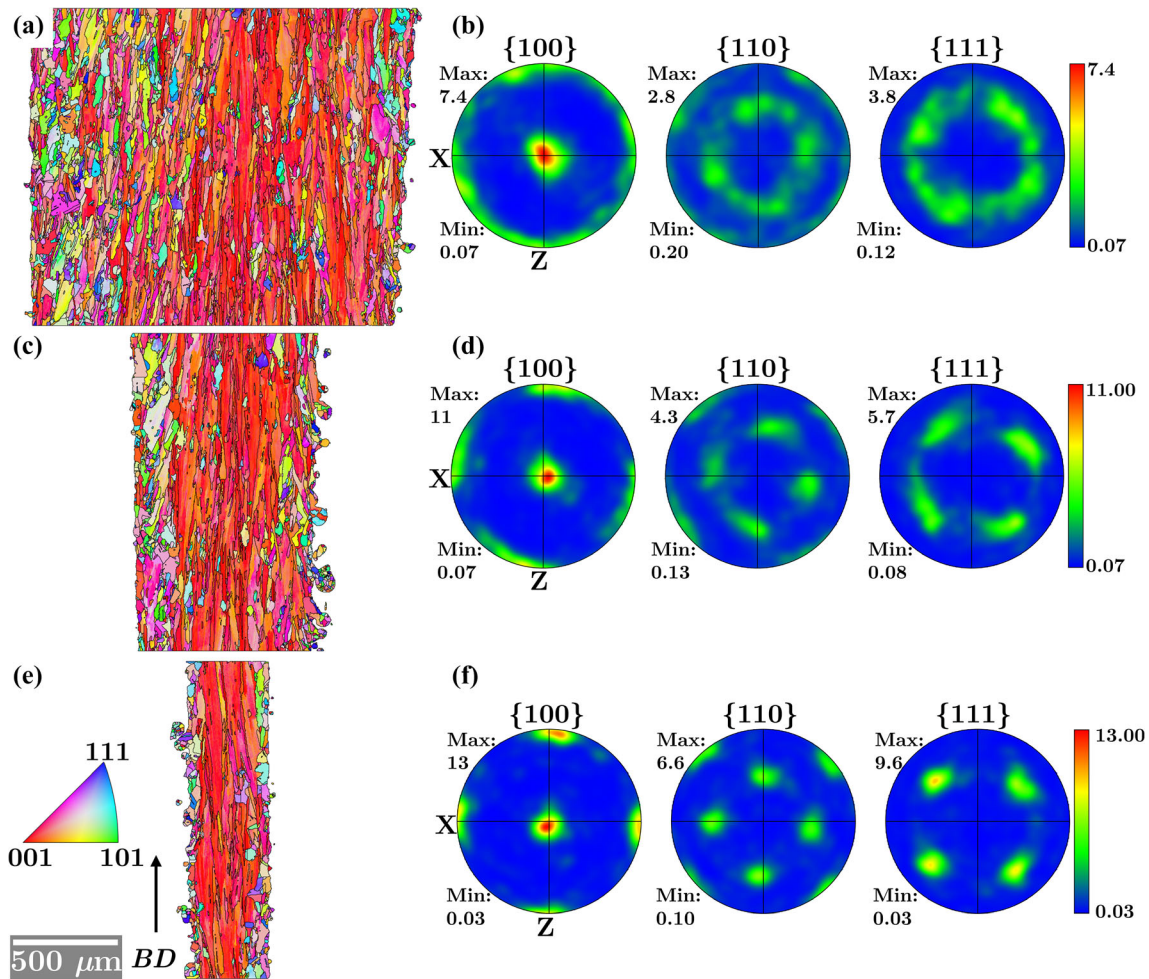
Fig. 8—EBSD orientation maps in inverse pole figure representation and the corresponding pole figures of IN-939 in heat-treated condition with 90 deg build angle of different thicknesses: (*a*, *b*) 2 mm thickness, (*c*, *d*) 1 mm thickness, and (*e*, *f*) 0.5 mm thickness. BD is build direction. BD is in the center for the pole figures. The orientation map is shown along BD and is given in IPF coloring. The color bar refers to the intensity of the pole figure (For interpretation of the references to color in this figure legend, the reader is referred to the web version of this article).

the thickness from 2 to 12 mm, there is minimal change in the texture. The only noticeable difference in texture occurs for thicknesses lower than 2 mm where the $\langle 100 \rangle$ intensity is found to increase due to the restricted heat dissipation. Table III summarizes the grain size measurement obtained from EBSD. The length of the major axis of the fitted ellipse is reported due to the presence of long columnar grains. The area-weighted mean, minimum, and the maximum length of the major axis of the fitted ellipse were reported along with the number of grains. Long columnar grains with length exceeding the analyzed area were not considered in the grain size analysis. The grains used for the grain size analysis covered about 57 to 68 and 79 to 86 pct for build angles of 90 and 45 deg, respectively. The area-weighted mean and the maximum length of the grains for parts with 90 deg build angle (as-built) increased when part thickness increased from 0.5 to 1 mm followed by a decrease for 2 mm. However, for 45 deg build angle (as-built), with increase in part thickness from 0.5 to 1 mm, the grain length increased in heat-treated condition (90 and 45 deg build angle). This was followed by a decrease in grain length when part thickness increased from

1 to 2 mm. The effect of part thickness on grain size is not clearly evident and would probably require further studies.

C. *Surface Topography and Roughness*

The 3D topography results obtained for different thicknesses (0.5, 1, and 2 mm) and different build angles (90 and 45 deg) are shown in Figure 11. The surface roughness parameters as per ISO 25718-2 standard[20] are shown in Figure 12. The measurements were performed on two surfaces (A) and (B) of the miniature tensile specimens. In Figure 12, both the surface roughness parameters for surfaces (A) and (B) for the same thickness are plotted. The surface roughness parameter with lower surface roughness value belongs to surface (B). It is observed that the surface (A) consists of sharp peaks indicated by the bright red color (Figure 11), which are primarily unmelted, or partially melted powder particles attached to the surface. For 90 deg build angle in case of surface (A), it is seen that the number of sharp peaks reduces as the thickness increases (Figure 11). While in 45 deg build angle in surface (A)
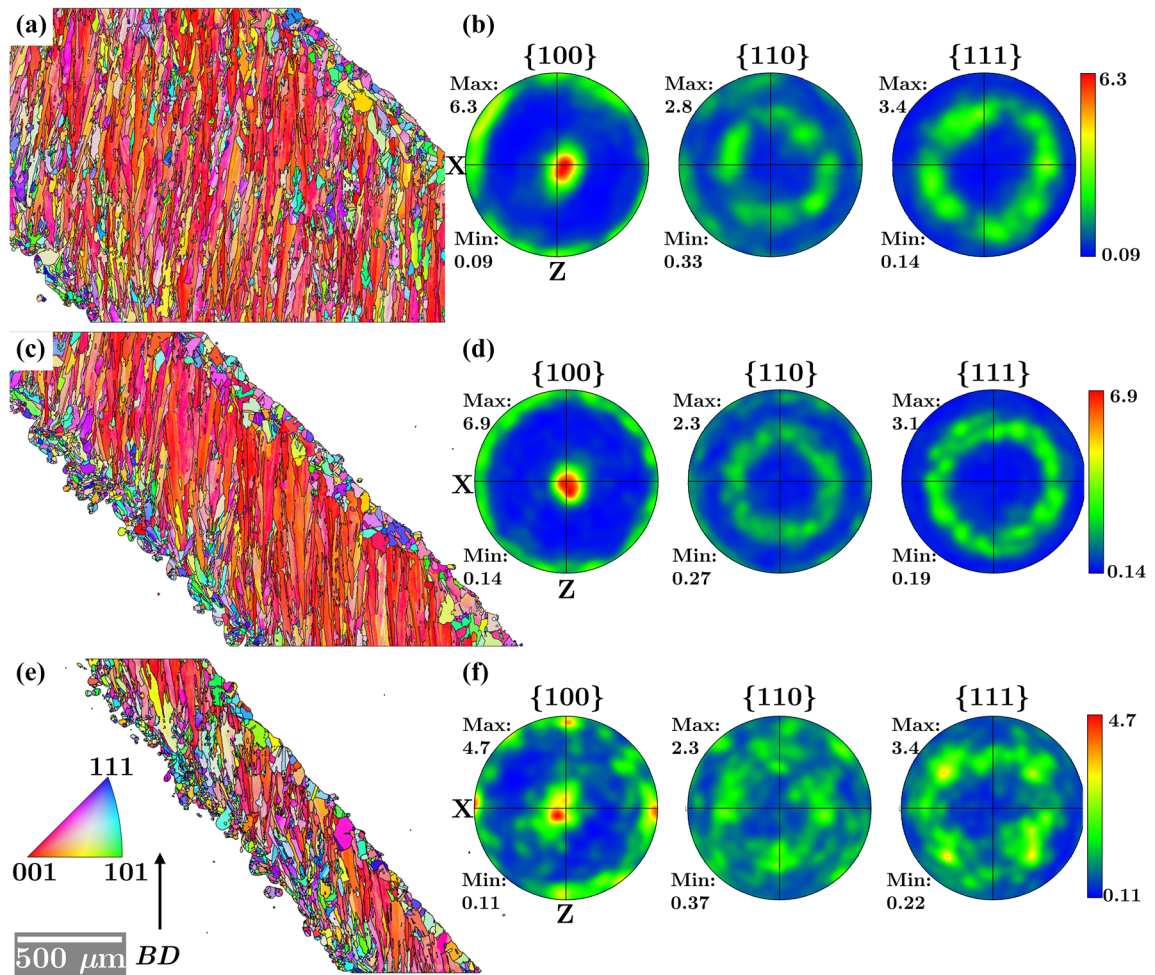
Fig. 9—EBSD orientation maps in inverse pole figure representation and the corresponding pole figures of IN-939 in heat-treated condition with 45 deg build angle of different thicknesses: (*a*, *b*) 2 mm thickness, (*c*, *d*) 1 mm thickness, and (*e*, *f*) 0.5 mm thickness. BD is build direction. BD is in the center for the pole figures. The orientation map is shown along BD and is given in IPF coloring. The color bar refers to the intensity of the pole figure (For interpretation of the references to color in this figure legend, the reader is referred to the web version of this article).

belonging to the downskin, the number of sharp peaks increases as the thickness increases (Figure 11). The same effect is also indicated by the surface roughness value with a more pronounced effect in S_k (core height) in Figure 12. For surface (B) in both 90 and 45 deg build angle samples, there is not a significant change either in surface topography (Figure 11) or in surface roughness parameters (Figure 12). The presence of some sharp peaks is indicative of some powder particles which are adhered/sintered to the surface (B). The presence of the staircase effect is also observed in the surface (B) for 45 deg build angle. Staircase effect is inherent to the layer-by-layer AM technologies where stair-like features are caused due to the chosen layer thickness.[30] This effect was not clearly observable on other surfaces due to the excessive amount of partly melted/sintered powder particles.

The reason for the difference in surface roughness arises from the difference in laser–powder interactions. The difference in the surface roughness of surface (A) and (B) for 90 deg build angle could arise due to the geometry and/or part placement in the build platform. The manufactured part which is a cooling panel for application in gas turbine

has internal channels as shown in Figures 1(b) and (c). It is possible that the adhered powder particles on surface facing outside (surface (B)) could detach from the surface during part handling. But it is highly unlikely the reason for the difference. The difference in the surface roughness is likely to be caused due to the difference in the laser behavior due to the part placement in the build platform. In an EOS M290 machine, used in this study, the laser beam incidence angle can change from 0 deg in the center to about 20 deg toward the corner of the build platform.[31] This results in a change in the laser focus geometry from spherical to oval and hence modified energy distribution in the laser focus and so difference in melt pool geometry. The difference in the laser beam incidence angle also causes the so-called melt extensions which are formed due to the improper connection between the liquid melt and the previously solidified layer. These melt extensions could cause the powder particles to be adhered to the surface differently.[31] This was unavoidable in this study as the build platform was packed with the parts to make efficient use of time and resources. With an inclined surface (for example, at 45 deg), the downskin usually has higher surface roughness which has been reported in previous studies.[24,32] The
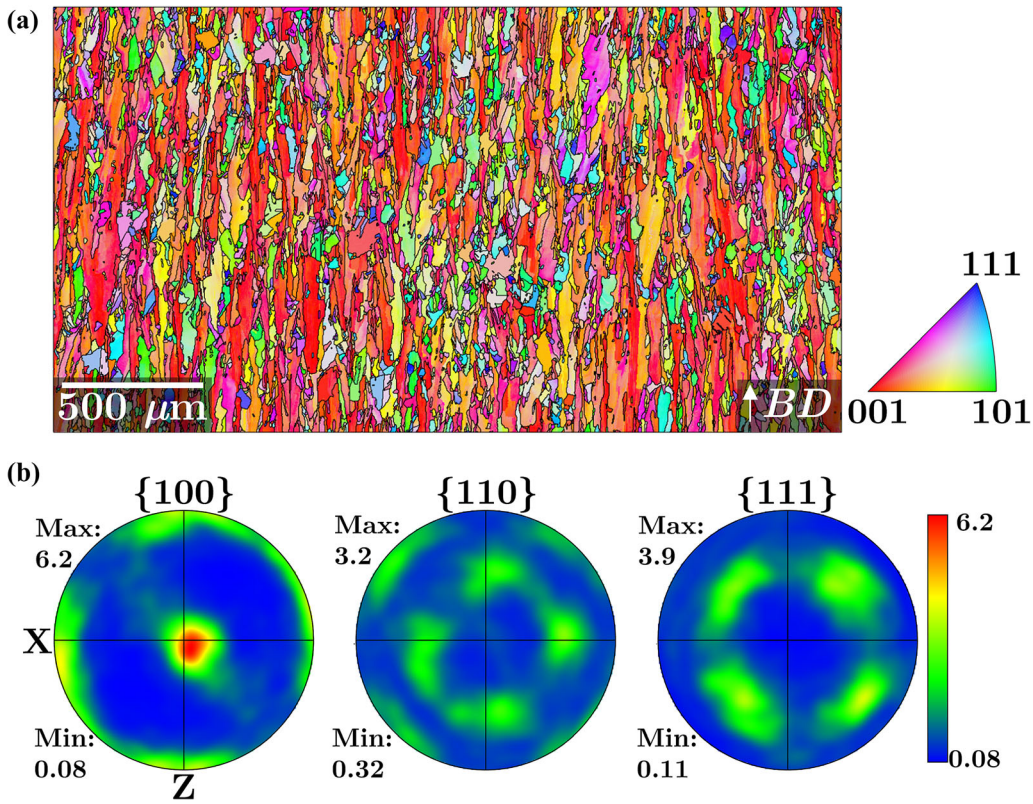
Fig. 10—EBSD orientation map in inverse pole figure representation and the corresponding pole figures of Standard IN-939 in heat-treated condition with 90 deg build angle of thickness 12 mm. BD is build direction. BD is in the center for the pole figures. The orientation map is shown along BD and is given in IPF coloring. The color bar refers to the intensity of the pole figure. (For interpretation of the references to color in this figure legend, the reader is referred to the web version of this article).
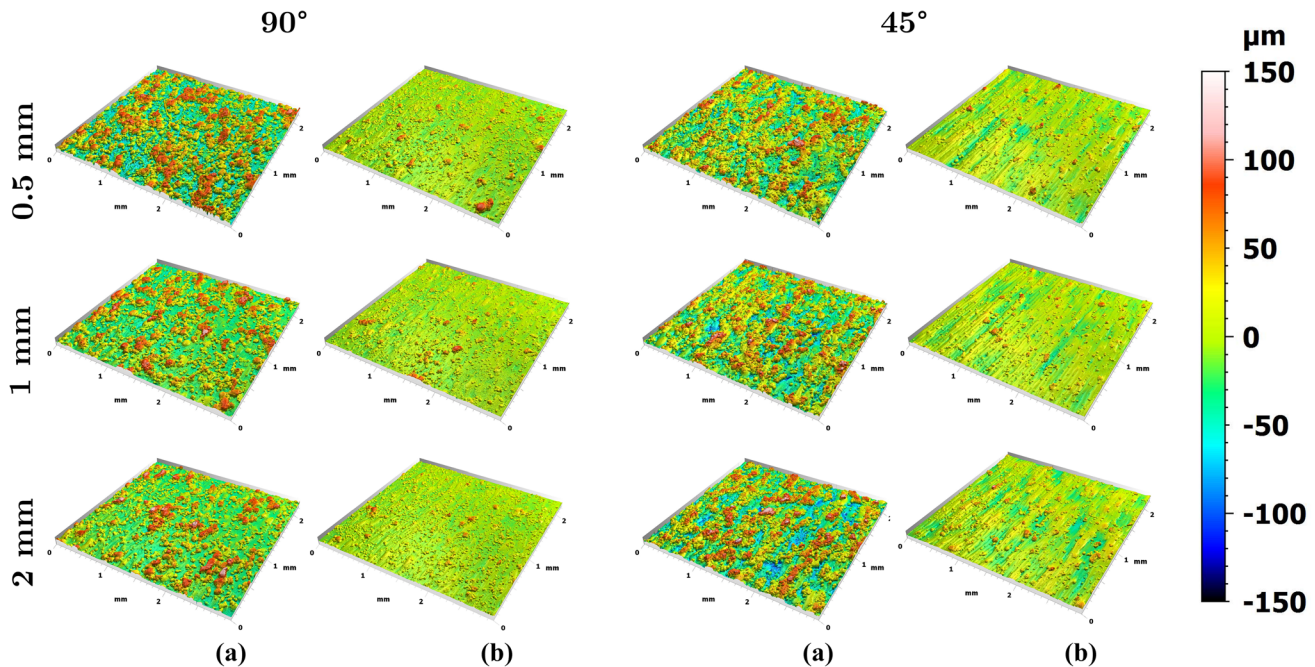

Fig. 11—3D topography obtained from confocal microscopy for both sides (*a*) and (*b*) of heat-treated IN-939 miniature tensile samples of different thicknesses (0.5, 1, and 2 mm) and build angle (90 and 45 deg). The scale bar shows the height of the different surfaces (For interpretation of the references to color in this figure legend, the reader is referred to the web version of this article).

downskin surface roughness is known to have poor local heat dissipation due to the powder having a lower conductivity caused by limited contact between the powder particles and the insulating air gaps between the powder particles.[24–26] The readily melted region in the downskin surface also seeps to the powder bed due to gravity. So, when a laser exposes the downskin, the powder particles adhere to the surface leading to higher surface roughness. This is indicated in Figure 6 by the higher fraction of the red powder particles in the downskin region for 45 deg build angle. This poor heat dissipation of the downskin coupled with gravity led to a higher surface roughness for parts with 45 deg build angle.

The variation of surface roughness parameters with part thickness has also been reported previously by Karlsson et al.[33] for Ti–6Al–4V manufactured by electron beam melting (PBF-EB/M).[34] PBF-EB/M processing is different from PBF-LB/M but is used for the sake of discussion. The reported results (measured by white lite interferometry, a non-contact optical method) showed that Ra (arithmetical mean height) was higher for the thinnest sample (0.5 mm) when compared to samples of higher thicknesses (1 to 5 mm) which is similar to the results obtained in this stu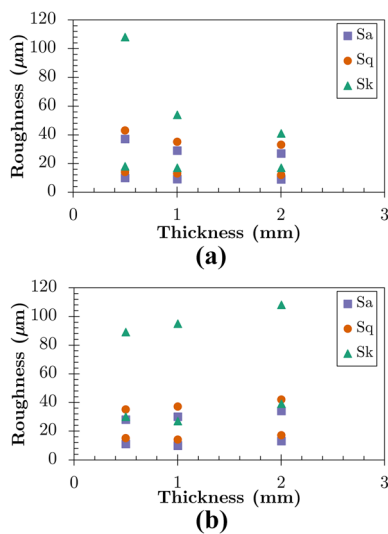dy. On the other hand, the reported surface roughness parameters (measured from cross-section LOM image) reported by Yu et al.[18] were not affected by variation in thickness (1 to 5 mm) for Hastelloy X manufactured by PBF-LB/M. But in another study (performed by use of μCT), Yu et al.[35] reported that roughness of a 1 mm wall thickness was slightly higher than that of a 2 mm wall thickness. The reason for this is the higher thermal gradient and heat accumulation in the bulk of the thin-wall samples with build angle of 90 deg[27] which could have led to more powder particles to attach to the surface. But the 45 deg build angle shows that the surface roughness increases when the part thickness increases (Figure 12(b)). At 45 deg build angle, the heat accumulation in the downskin increases with the increase in part thickness. This leads to more powder particles attached in the downskin resulting in a higher surface roughness.

Fig. 12—Surface roughness parameters of specimens with different thicknesses with build angle of (a) 90 deg and (b) 45 deg. S_a Arithmetical mean height, S_q Root mean square height, S_k Core height. Parameters for both surface (a) and (b) are plotted at the same thickness.
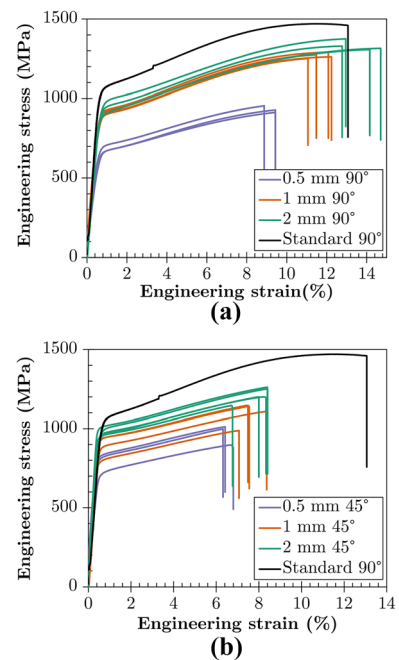

Fig. 13—(a) Engineering stress–strain curve of specimens with 90 deg build angle and (b) Engineering stress–strain curve of specimen with 45 deg build angle. Method 1 thickness was used for the cross-section area.

Table IV. Tensile Properties Obtained for the Specimens Used in This Study

Thickness (mm)	Build Angle (Deg)	Yield Strength (MPa)	UTS (MPa)	Total Elongation at Fracture (Pct)
0.5	90	699 ± 20	932 ± 21	9.24 ± 0.33
1	90	933 ± 11	1269 ± 16	11.71 ± 0.55
2	90	987 ± 25	1331 ± 30	13.64 ± 0.93
0.5	45	808 ± 41	955 ± 60	6.61 ± 0.33
1	45	942 ± 26	1134 ± 18	7.52 ± 0.69
2	45	986 ± 29	1204 ± 58	7.93 ± 0.80
7	90	1051 ± 11	1482 ± 9	13.70 ± 2.50

D. Tensile Properties and Stress Calibration

The tensile test curves obtained in this study from miniature tensile specimens along with the tensile curve from the 'Standard' specimen are shown in Figures 13(a) and (b). The yield strength (0.2 pct offset), UTS, and the elongation at fracture are summarized in Table IV. The elongation at fracture is the tensile strain at fracture (in pct) obtained from the extensometer. Since the extensometer was attached to the sample until fracture, this leads to accurate elongation values. The cross-sectional area for stress calculations used the thickness measurements from Method 1 (caliper). The tensile results of two 'Standard' specimens are also reported. The 0.5 mm thick specimen with 90 deg build angle was found to have the lowest yield strength with a value of 699 ± 20 MPa. But the specimens of 1 and 2 mm thickness had similar yield strength with a value of 933 ± 11 and 987 ± 25 MPa, respectively. The elongation at fracture was found to increase with the increase in thickness of the specimens. The yield strength and the UTS of the miniature specimens were inferior to the 'Standard' specimen. However, it is observed that the elongation at fracture for the thickest wall $(13.64 \pm 0.93$ pct) is similar to the 'Standard' specimen $(13.70 \pm 2.50$ pct). For specimens with build angle of 45 deg, the yield strength, UTS, and the elongation at fracture were also found to increase with the increase in the specimen thickness. However, the elongation at fracture was about 42 to 50 pct lower than the 'Standard' specimen. In general, the yield and tensile strength are lower than the 'Standard' specimens.

The influence of part thickness on tensile properties have been studied previously for SS316L,[13,16] HX[18,36] and Ti–6Al–4V[33,37] manufactured by PBF (powder bed fusion). Results have shown that YS, UTS, and the elongation at fracture increase when the sample thickness increased. Also, studies where the materials were manufactured by conventional manufacturing techniques also covered the effect of thickness on tensile properties.[38–40] Yang et al.[38] studied pure Cu manufactured by electron beam melting (EBM) and friction stir processing (FSP). The samples were ground and polished to remove surface defects. The yield strength was not affected by increasing the sample thickness (100 μm to 2 mm for EBM and 100 μm to 0.5 mm for FSP). UTS and the elongation to fracture improved when the sample thickness increased. The UTS, however, reached a saturated stage and became constant when the thickness (t) and grain size (d) ratio, hereafter referred to as t/d, was larger than a critical value. The critical t/d is material-dependent and was reported to be 6 to 18 for Cu,[38] 6 to 10 for ferrous materials,[40] 4 to 5 for Al[41] and ~ 5 for IN-718.[42] Apart from the critical t/d, there is also aspect ratio (AR, specimen thickness to width ratio) and slimness ratio (ratio of gauge length to square root of cross-section area) which can have effect on tensile properties.[40,43] An aspect ratio greater than 0.2 and slimness ratio of around 5.65 is acceptable for the miniature tensile specimen to get tensile properties similar to the bulk standard specimen.[44]

Table V. Thickness to Grain Size (t/d) ratio, Aspect Ratio (AR), and the Slimness Ratio for the Samples Tested in this Study

Thickness (mm)	Build Angle (Deg)	t/d (—)	AR (—)	Slimness Ratio (—)
0.5	90	21.76	0.16	10.2
1	90	43.27	0.33	7.21
2	90	81.56	0.66	5.10
0.5	45	23.58	0.16	10.2
1	45	42.99	0.33	7.21
2	45	85.54	0.66	5.10
7	90	287.79	1	5

Table VI. Different Thickness Measurements Obtained Through Three Different Methods Used to Calculate the Yield Strength (0.2 Pct Offset)

CAD Thickness (mm)	Build Angle (Deg)	Method 1 (mm)	Method 2 (mm)	Method 3 (mm)
0.5	90	0.56	0.39	0.48
1	90	1.05	0.82	0.98
2	90	2.03	1.84	1.98
0.5	45	0.64	0.41	0.52
1	45	1.1	0.86	0.98
2	45	2.08	1.82	1.93

Method 1 = Caliper, Method 2 = LOM and Method 3 = Surface roughness.

The calculated t/d, aspect ratio, and slimness ratio of the specimens tested in this study are shown in Table V. It is observed that the calculated parameters are mostly within the acceptable limits with only the slimness ratio having some unacceptable values. However, the tests done by Zhang et al.[43] for a range of steels showed that the YS and UTS were similar when these parameter ratios changed. However, the elongation at fracture was influenced by these parameter ratios. The elongation was higher when the slimness ratio was lower and aspect ratio was higher. This behavior of elongation is also similar to the results from this study. Using finite element modeling, Yuan et al.[39] found that the increased elongation in higher thickness samples was due to the increased size of the region where the stress is above the yield stress, which increases when the specimen thickness increased. Similar elongation behavior has also been reported in previous studies.[13,14] Inferior elongation to fracture for samples with build angle lower than 90 deg has been previously reported.[22] Deng et al.[22] reported that the difference in mechanical properties with different build angles in as-built condition was affected by the different residual stresses and dislocation density. With heat treatment, the difference in mechanical properties is reduced due to the relief of residual stresses and dislocation recovery. In this study, it is safe to assume that the residual stress is relieved due to the heat treatment. However, the dislocation density was not within the scope of this study. Also, the loading of the grains is different for the specimens of 90 and

Table VII. Comparison of the Yield Strength (YS) Obtained from Method 1 (Caliper), Method 2 (LOM), and Method 3 (Roughness)

Thickness (mm)	Build (Deg)	Angle	YS Method 1 (MPa)	Method 2 (MPa)	Method 3 (MPa)	UTS Method 1 (MPa)	Method 2 (MPa)	Method 3 (MPa)
0.5	90		699 ± 20	1073 ± 24	863 ± 28	1028 ± 16	1484 ± 18	1165 ± 15
1	90		933 ± 11	1115 ± 5	985 ± 3	1247 ± 19	1553 ± 7	1361 ± 6
2	90		987 ± 25	1031 ± 40	961 ± 53	1322 ± 41	1470 ± 37	1374 ± 33
0.5	45		808 ± 41	1169 ± 36	984 ± 30	1074 ± 43	1388 ± 59	1172 ± 50
1	45		942 ± 26	1195 ± 18	1059 ± 24	1130 ± 29	1450 ± 14	1285 ± 12
2	45		986 ± 29	1116 ± 46	1052 ± 44	1206 ± 70	1376 ± 82	1296 ± 76
7	90		1051 ± 11	—	—	1482 ± 9	—	—

45 deg build angles. For 90 deg build angle, the tensile loading is parallel to the BD with a strong ⟨100⟩ texture. While for 45 deg build angle, the difference between the tensile loading direction and ⟨100⟩ direction is 45 deg. The difference in the loading direction with the preferential texture could also have led to the lower elongation in the 45 deg sample.

PBF-LB surfaces are known to have higher surface roughness.[13] Hence, using caliper to measure the thickness (Method 1) was believed to be an overestimation of the load-bearing area. Table VI shows a comparison of the thickness measured from three different methods as explained in Section II–C. CAD (computer-aided design) thickness refers to the intended thickness which was used in the CAD model. It is seen that Method 1 (measured using caliper) gives larger apparent thickness. However, this is necessarily not the true thickness. Method 1 measures the bulk along with the surface roughness caused by unmelted or semi-melted particles attached to the surface. This overestimates the load-bearing cross-sectional area leading to lower YS and UTS. Method 2 and Method 3 were two ways used to find the true cross-sectional area. Method 2 used LOM image to find the true thickness while excluding the surface roughness. Method 3 used the S_k surface roughness parameter (Section III–C) for the surfaces (A) and (B) which was then subtracted from the apparent thickness from Method 1 to obtain the true thickness. The reason for using S_k is because it is the core depth which is obtained by subtracting height of predominant peak with predominant trough. It was also found that S_k was varying for the different wall thicknesses.

The apparent YS (Method 1) and the corrected YS (Method 2 and Method 3) are shown in Figure 14 and Table VII. The YS was found to decrease with the decrease in thickness (Method 1). This apparent effect of thickness arises from the additional surface roughness measured using caliper. Similar results have also been reported in previous studies.[13,18] However, for Method 2 and Method 3, the YS increases for respective thickness values. This is caused by using a corrected thickness which is lower than the apparent thickness measured in Method 1. Comparing the deviation in pct of YS values of different thicknesses from Method 1, Method 2, and Method 3 to the 'Standard' specimen, it
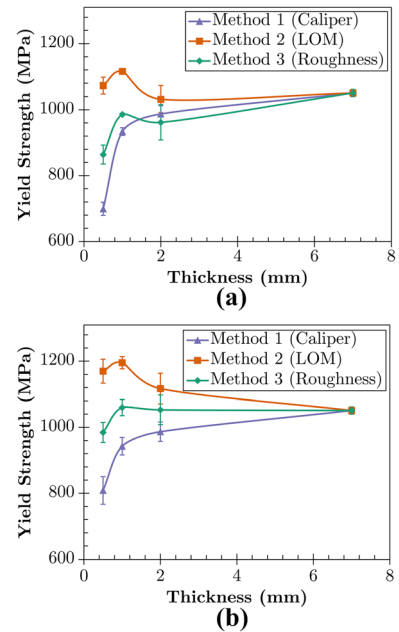

Fig. 14—Yield strength (YS) from Method 1, Method 2, and Method 3 for build angle of (a) 90 deg and (b) 45 deg.

is seen that deviation in YS from Method 1, Method 2, and Method 3 was 6 to 33, 1 to 13, and 0.2 to 17 pct, respectively. Clearly, the deviation is higher in Method 1 than in Method 2 and Method 3. This shows that Method 2 and Method 3 are good for calibrating the errors in thickness measurement for tensile testing specimens with as-built surfaces. Furthermore, comparing the YS of the miniature specimens with the 'Standard' specimen provides a maximum deviation of 13 and 17 pct for Method 2 and Method 3, respectively. Zhang et al.[43] reported that if the error between the miniature specimens and the standard specimens is within 15 pct, the mechanical properties are a good estimate. This shows that the corrected tensile properties of the miniature tensile specimens with thin walls are comparable to the 'Standard' specimen.

IV. CONCLUSION

In the current study, precipitation-strengthened superalloy (IN-939) parts were built with varying thickness (0.5, 1, and 2 mm) using PBF-LB/M. The parts were built vertically (90 deg build angle) and with an incline (45 deg build angle). The texture was analyzed in the as-built and heat-treated condition. The mechanical response of heat-treated IN-939 was studied using tensile testing. A correction for the yield strength was proposed based on the true thickness obtained through light optical microscopy and surface roughness measurements. The following are the significant findings from this study:

1. A strong $\langle 100 \rangle$ texture along the build direction (BD) was found in both the as-built and heat-treated condition. This is due to the dominant thermal gradient along the BD. The heat treatment caused no change in the overall texture.
2. The $\langle 100 \rangle$ texture intensity increased for 90 deg build angle as the part thickness decreased. This is due to the thermal gradient being affected by part thickness. In 90 deg build angle, the thermal gradient is higher in thin walls which leads to predominantly $\langle 100 \rangle$ columnar grains. For thick wall, the fraction of grains with crystallographic orientations other than $\langle 100 \rangle$ is present which decreases the overall crystallographic texture intensity.
3. The $\langle 100 \rangle$ texture intensity decreased for 45 deg build angle as the part thickness decreased. This arises from the contribution of partly melted/ sintered powder particles in the downskin surface with different crystallographic orientations. As the part thickness increases, there are relatively more $\langle 100 \rangle$ columnar grains in the bulk than the powder particles on the downskin. This leads to a higher crystallographic texture intensity in thick walls than thin walls.
4. The small grains with random crystallographic orientations found at the upskin for 45 deg build angle come from the powder particles having fine grains which were remelted during the contour scan. These small grains underwent grain growth during the heat treatment.
5. The surface roughness was found to decrease as the part thickness increased for 90 deg build angle and *vice versa* for 45 deg build angle. This is due to the difference in heat accumulation for both the build angles. For 90 deg build angle with thin walls, the heat accumulation is higher leading to more partly melted/sintered powder particles attached to the surface. For 45 deg build angle, the thick walls have high heat accumulation in the downskin along with the poor heat dissipation of the powder bed which led to a higher surface roughness in the downskin surface.
6. The yield strength (YS) and ultimate tensile strength (UTS) values of the miniature specimens with part thickness of 0.5 mm were inferior to the specimens with part thickness of 1 and 2 mm. This was due to the overestimation of the load-bearing area caused due to the measurement with caliper (Method 1) which measured the bulk thickness and the surface roughness.
7. Two types of correction to find the true thickness were reported: (a) using LOM image to find the bulk thickness (Method 2) and (b) using surface roughness parameter S_k to find the bulk thickness (Method 3). Method 2 and Method 3 gave YS values which had a maximum deviation of about 13 and 17 pct, respectively, in comparison with YS of the 'Standard' specimen which had YS of 1051 ± 11 MPa. For UTS, the maximum deviation of Method 2 and Method 3 was about 5 and 21 pct, respectively, in comparison with the UTS of the 'Standard' specimen which had a UTS of 1482 ± 9 MPa. Method 2 (LOM) seemed to give the lowest deviation and the best way to obtain corrected stresses.

CONFLICT OF INTEREST

On behalf of all authors, the corresponding author states that there is no conflict of interest.

REFERENCES

1. W.E. Frazier: *J. Mater. Eng. Perform.*, 2014, vol. 23, pp. 1917–28.
2. Z. Wu, S.P. Narra, and A. Rollett: *Int. J. Adv. Manuf. Technol.*, 2020, vol. 110, pp. 191–207.
3. ISO/ASTM: *ISO/ASTM 52911-1:2019, Additive Manufacturing – Design – Part 1: Laser-based Powder Bed Fusion of Metals*, 2019.
4. A. Leicht, U. Klement, and E. Hryha: *Mater. Charact.*, 2018, vol. 143, pp. 137–43.
5. S.S. Babu, N. Raghavan, J. Raplee, S.J. Foster, C. Frederick, M. Haines, R. Dinwiddie, M.K. Kirka, A. Plotkowski, Y. Lee, and R.R. Dehoff: *Metall. Mater. Trans. A*, 2018, vol. 49A, pp. 3764–80.
6. T. DebRoy, H.L. Wei, J.S. Zuback, T. Mukherjee, J.W. Elmer, J.O. Milewski, A.M. Beese, A. Wilson-Heid, A. De, and W. Zhang: *Prog. Mater. Sci.*, 2018, vol. 92, pp. 112–224.
7. S. Sanchez, P. Smith, Z. Xu, G. Gaspard, C.J. Hyde, W.W. Wits, I.A. Ashcroft, H. Chen, and A.T. Clare: *Int. J. Mach. Tools Manuf.*, 2021, vol. 165, p. 103729.
8. A. Bridges, J. Shingledecker, A. Torkaman, and L. Houck: *Proc. ASME Turbo Expo*, 2020, vol. 8, pp. 1–10.
9. T.B. Gibbons and R. Stickler: in *High Temperature Alloys for Gas Turbines*, R. Brunetaud, D. Coutsouradis, T.B. Gibbons, Y. Lindblom, D.B. Meadowcroft, and R. Stickler, eds., Springer Netherlands, Dordrecht, 1982, pp. 369–93.
10. G. Wang: in *Precision Forming Technology of Large Superalloy Castings for Aircraft Engines*, B. Sun, J. Wang, and D. Shu, eds., Springer Singapore, Singapore, 2021, pp. 33–65.
11. T.S. Piwonka: in *Materials Selection and Design*, G.E. Dieter, ed., vol. 20, ASM Handbook, 1997, pp. 723–29.
12. Electro Optical Systems GmbH - EOS Additive Manufacturing: *EOS NickelAlloy IN939 (Material Data Sheet)*, 2021.
13. A. Leicht, C. Pauzon, M. Rashidi, U. Klement, L. Nyborg, and E. Hryha: *Adv. Ind. Manuf. Eng.*, 2021, vol. 2, p. 100037.
14. X. Wang, J.A. Muñiz-Lerma, O. Sánchez-Mata, M. Attarian Shandiz, and M. Brochu: *Mater. Sci. Eng. A*, 2018, vol. 736, pp. 27–40.
15. X. Wang, J.A. Muñiz-Lerma, O. Sanchez-Mata, M. Attarian Shandiz, N. Brodusch, R. Gauvin, and M. Brochu: *Scripta Mater.*, 2019, vol. 163, pp. 51–56.
16. O. Sanchez-Mata, X. Wang, J.A. Muñiz-Lerma, S.E. Atabay, M. Attarian Shandiz, and M. Brochu: *J. Alloys Compd.*, 2022, vol. 901, p. 163465.
17. C.-H. Yu, R.L. Peng, M. Calmunger, V. Luzin, H. Brodin, and J. Moverare: in *Superalloys 2020*, S. Tin, M. Hardy, J. Clews, J. Cormier, Q. Feng, J. Marcin, C. O'Brien, and A. Suzuki, eds., Springer International Publishing, Cham, 2020, pp. 1003–13.
18. C.H. Yu, R.L. Peng, V. Luzin, M. Sprengel, M. Calmunger, J.E. Lundgren, H. Brodin, A. Kromm, and J. Moverare: *Addit. Manuf.*, 2020, vol. 36, p. 101672.
19. F. Bachmann, R. Hielscher, and H. Schaeben: *Solid State Phenom.*, 2010, vol. 160, pp. 294–306.
20. International Organisation for Standardization: *ISO 25178-2:2012, Geometrical Product Specifications (GPS) — Surface Texture: Areal — Part 2: Terms, Definitions and Surface Texture Parameters*, vol. 25178-2:20, 2012.
21. P. Kanagarajah, F. Brenne, T. Niendorf, and H.J. Maier: *Mater. Sci. Eng. A*, 2013, vol. 588, pp. 188–95.
22. D. Deng, R.L. Peng, H. Brodin, and J. Moverare: *Mater. Sci. Eng. A*, 2018, vol. 713, pp. 294–306.
23. S. Banoth, C.W. Li, Y. Hiratsuka, and K. Kakehi: *Metals (Basel)*, 2020, vol. 10, pp. 1–16.
24. Z. Chen, X. Wu, D. Tomus, and C.H.J. Davies: *Addit. Manuf.*, 2018, vol. 21, pp. 91–103.
25. A.V. Gusarov and E.P. Kovalev: *Phys. Rev. B*, 2009, vol. 80, pp. 16–20.
26. M. Rombouts, L. Froyen, A.V. Gusarov, E.H. Bentefour, and C. Glorieux: *J. Appl. Phys.*, 2005, vol. 97, p. 024905.
27. S.I. Shahabad, U. Ali, Z. Zhang, A. Keshavarzkermani, R. Esmaeilizadeh, A. Bonakdar, and E. Toyserkani: *J. Manuf. Process.*, 2022, vol. 75, pp. 435–49.
28. P. Pant, F. Salvemini, S. Proper, V. Luzin, K. Simonsson, S. Sjöström, S. Hosseini, R. Lin Peng, and J. Moverare: *Mater. Des.*, 2022, vol. 214, p. 110386.
29. A.S. Shaikh: Chalmers University of Technology, 2018.
30. F. Calignano: *Virtual Phys. Prototyp.*, 2018, vol. 13, pp. 97–104.
31. S. Rott, A. Ladewig, K. Friedberger, J. Casper, M. Full, and J.H. Schleifenbaum: *Addit. Manuf.*, 2020, vol. 36, p. 101437.
32. J.C. Snyder and K.A. Thole: *J. Manuf. Sci. Eng. Trans. ASME*, 2020, vol. 142, p. 071003.
33. J. Karlsson, T. Horn, H. West, R. Aman, A. Snis, H. Engqvist, J. Lausmaa, and O. Harrysson: *Addit. Manuf.*, 2016, vol. 12, pp. 45–50.
34. ISO/ASTM: *ISO/ASTM DIS 52911-3 Additive Manufacturing — Design — Part 3: Electron Beam Powder Bed Fusion of Metals*, 2019.
35. C.H. Yu, A. Leicht, R.L. Peng, and J. Moverare: *Mater. Sci. Eng. A*, 2021, vol. 821, p. 141598.
36. O. Sanchez-Mata, X. Wang, J.A. Muñiz-Lerma, S.E. Atabay, M. Attarian Shandiz, and M. Brochu: *J. Alloys Compd.*, 2021, vol. 865, p. 158868.
37. J. Dzugan, M. Sei, R. Prochazka, M. Rund, P. Podany, P. Konopik, and J.J. Lewandowski: *Addit. Manuf.*, 2018, vol. 143, pp. 94–109.
38. L. Yang and L. Lu: *Scripta Mater.*, 2013, vol. 69, pp. 242–45.
39. W.J. Yuan, Z.L. Zhang, Y.J. Su, L.J. Qiao, and W.Y. Chu: *Mater. Sci. Eng. A*, 2012, vol. 532, pp. 601–05.
40. A. Kohyama, K. Hamada, and H. Matsui: *J. Nucl. Mater.*, 1991, vol. 179–181, pp. 417–20.
41. H. Liu, Y. Shen, J. Ma, P. Zheng, and L. Zhang: *J. Mater. Eng. Perform.*, 2016, vol. 25, pp. 3599–3605.
42. B.B. Liu, J.Q. Han, R. Zhao, W. Liu, and M. Wan: *Nanomaterials*, 2016, vol. 35, pp. 989–98.
43. L. Zhang, W. Harrison, M.A. Yar, S.G.R. Brown, and N.P. Lavery: *J. Mater. Res. Technol.*, 2021, vol. 15, pp. 1830–43.
44. ISO: *ISO 6892-1:2016, Metallic Materials — Tensile Testing — Part 1: Method of Test at Room Temperature*, 2016.